Metal-Organic Framework Glasses with Permanent Accessible Porosity

Chao Zhou,[1,2] Louis Longley,[1] Andraž Krajnc,[3] Glen J. Smales,[4,5] Ang Qiao,[6] Ilknur Eruçar,[7] Cara M. Doherty,[8] Aaron W. Thornton,[8] Anita J. Hill,[8] Christopher W. Ashling,[1] Omid T. Qazvini,[9] Seok J. Lee,[9] Philip A. Chater,[5] Nicholas J. Terrill,[5] Andrew. J. Smith,[5] Yuanzheng Yue,[2,6,10] Gregor Mali,[3] David A. Keen,[11] Shane G. Telfer[9] and Thomas D. Bennett*[1]*

[1]*Department of Materials Science and Metallurgy, University of Cambridge, Charles Babbage Road, Cambridge, CB3 0FS, UK*

[2]*Department of Chemistry and Bioscience, Aalborg University, DK-9220 Aalborg, Denmark*

[3]*Department of Inorganic Chemistry and Technology, National Institute of Chemistry, SI-1001 Ljubljana, Slovenia*

[4]*Department of Chemistry, University College London, Gordon Street, London, WC1H 0AJ, UK*

[5]*Diamond Light Source Ltd, Diamond House, Harwell Science and Innovation Campus, Didcot OX11 0DE, UK*

[6]*State Key Laboratory of Silicate Materials for Architectures, Wuhan University of Technology, Wuhan 430070, China*

[7]*Department of Natural and Mathematical Sciences, Faculty of Engineering, Ozyegin University, Istanbul, Turkey*

[8]*Future Industries, Commonwealth Scientific and Industrial Research Organisation, Clayton South, Victoria 3168, Australia*

[9] *MacDiarmid Institute for Advanced Materials and Nanotechnology, Institute of Fundamental Sciences, Massey University, Palmerston North 4442,* New Zealand

[10] *School of Materials Science and Engineering, Qilu University of Technology, Jinan 250353, China*

[11]*ISIS Facility, Rutherford Appleton Laboratory, Harwell Campus, Didcot, Oxon OX11 0QX, UK*

Email: tdb35@cam.ac.uk S.Telfer@massey.ac.nz

Abstract

To date, only several microporous, and even fewer nanoporous, glasses have been produced, always via post synthesis acid treatment of phase separated dense materials, e.g. Vycor glass. In comparison, high internal surface areas are readily achieved in crystalline materials, such as metal-organic frameworks (MOFs). It has recently been discovered that a new family of melt quenched glasses can be produced from MOFs, though they have thus far have lacked the accessible and intrinsic porosity of their crystalline precursors. Here, we report the first glasses that are permanently, and reversibly porous toward incoming gases, without post-synthetic treatment. We characterized the structure of these glasses using a range of experimental techniques, and demonstrate pores in the range of 4 – 8 Å. The discovery of MOF glasses with permanent accessible porosity reveals a new category of porous glass materials that are potentially elevated beyond conventional inorganic and organic porous glasses by their diversity and tunability.

Conventional porous glasses are silica-rich materials derived by acid treatment of phase-separated borosilicate glass precursors. They have found widespread applications in electrodes, chromatography and medical devices, and as desiccants, coatings and membranes.[1] In general, they are easily processed and exhibit high mechanical stability. However, these advantages are offset by limitations in their pore sizes, which are typically confined to the macroporous size regime. No porous glass has been fabricated directly by melt-quenching, without post-treatment. Few microporous glasses have been reported, although advances in their synthesis would be particularly attractive for applications based on the selective uptake of gases and small molecules.[2] One of the most well studied microporous glasses is Vycor, which is obtained by first melt-quenching a borosilicate liquid, and then heat treating the glass at a temperature well above T_g, to encourage phase separation. The borate-rich phase is then leached out via acid treatment, to generate pores of approximately 3 nm radii and Brunauer-Emmett-Teller (BET) surface areas in the range 100-200 m^2g^{-1}.[1] Silica-derived aerogels have also attracted much attention due to their own high BET surface areas and pore sizes of between 0.5 nm and 1 nm.[3] The desire to introduce controllable properties based on organic functional groups has however also spurred the development of amorphous microporous organic materials, such as PIM-1.[4,5] Surface areas verging on 1000 m^2g^{-1} arising from pore sizes of up to 1 nm have been reported. Whilst these organic materials present fewer chemical restrictions on their functionality than their inorganic counterparts, their thermal stability is unfortunately limited and their susceptibility to densification over time (physical aging) is well documented.[5]

In this context, porous materials that combine the advantageous properties of both inorganic and organic glasses are highly sought after. Recent advances in our understanding of the flexible behaviour[6] of soft porous metal-organic frameworks (MOFs)[7] have combined with a surge in research into defects[8] and disorder[9] to redefine our perception of MOFs as 'perfect' crystalline materials.[10] We, and others, have drawn on these advances to show that

crystallinity is not a prerequisite for many of the attractive properties of MOFs, and to produce liquids and glasses with internal cavities and ion conducting abilities.[11-13]

One lineage of MOFs that has garnered much attention is the zeolitic imidazolate framework (ZIF) family, numbering over 140 distinct structures containing tetrahedral transition metal ions, linked by imidazolate bis(monodentate) ligands into zeolitic architectures.[14,15] Several members of the family melt upon heating to around 400 °C. For example, in the case of certain polymorphs of ZIF-4 ([$Zn(Im)_2$], Im = imidazolate, $C_3H_3N_2^-$), this process proceeds on a sub-nanosecond timescale near T_m (melting temperature) and results in a viscous MOF liquid of identical chemical composition to the crystalline solid.[11] Quenching of the liquid results in a 'frozen' structure containing tetrahedral Zn(II) ions bridged by Im ligands. The continuous random network produced is similar to that of *a*SiO_2, but with the advantage of having both inorganic and organic components.[11,16] Known hybrid glasses, formed from ZIFs and phosphate coordination polymers,[17,18] are all inaccessible to guest molecules.

Motivated by the prospect of combining the attractive properties of both inorganic and organic moieties in a porous glass, we sought, for the first time, to develop *accessible* porosity in a melt-quenched MOF. We herein report the successful realization of this goal, in the form of glasses derived from ZIFs that reversibly adsorb gas molecules. These materials can be considered prototypical new porous glasses, given that there is no requirement for post-processing treatment. They are synthesized using a straightforward protocol and are stable, retaining their porosity in air over extended periods. Structure-property relationships are drawn between the composition of the material, glass and melting transition temperatures (T_g and T_m), and pore volume. These results provide a rational strategy upon which other porous MOF liquid and glass systems can be produced. We anticipate that the stability, processability and chemical diversity of these glasses will underpin their applications in separations, and as components of membranes, catalysts, functional coatings, and thin films.

Results and Discussion

Thermal characterization and vitrification of ZIF precursors

The free energy requirement for breaking the zinc-imidazolate bond has been calculated to be *ca*. 92 kJ mol^{-1} at 865 K.[11] This relatively low bond strength led us to consider ZIFs containing this ligand as primary candidates for melting, followed by quenching of the liquid to produce porous glasses. Limitations exist to the exclusive use of imidazolate however, since close association of the Zn and Im components in the liquid and glass states leads to dense materials.[16] We thus developed a strategy involving the incorporation of sterically congested benzimidazolate (bIm) ligands into the framework, alongside the parent imidazolate linker. We anticipated that the inclusion of a bulky ligand would prevent close packing of the liquid state upon melting, and therefore facilitate pore network formation upon quenching. Similar approaches have proven successful in optimizing porosity in both crystalline materials,[19] and amorphous organic polymers.[5] Suitable levels of the imidazolate linker are however still required to facilitate melting, since frameworks constructed exclusively from benzimidazolate ligands do not melt.

To develop our strategy, we initially focused on ZIF-76, $[Zn(Im)_{1.62}(5\text{-ClbIm})_{0.38}]$ (5-ClbIm = 5-chlorobenzimidazolate, $C_7H_4N_2Cl$) (**Figure 1a**).[20] The structure possesses a framework density of 1.03 T/nm^{-3} (T = tetrahedral metal atoms). This is extremely low when compared with ZIF-4 (3.66 T/nm^{-3}), which forms a non-porous glass, and ZIF-8 $[Zn(mIm)_2]$, (mIm = 2-methylimidazolate, $C_3H_5N_2^-$) (2.45 T/nm^{-3}), which does not melt.[21] The structure of ZIF-76 was confirmed by powder X-ray diffraction (PXRD), and the Im:5-ClbIm ratio determined by ^{1}H nuclear magnetic resonance (NMR) spectroscopy on dissolved samples. Desolvation of ZIF-76 resulted in loss of occluded 5-ClbIm from the pores (**Supplementary Figures 1-5**).

Thermogravimetric analysis (TGA) performed on an evacuated sample of ZIF-76 under argon resulted in a featureless trace until thermal decomposition at 525 °C. An accompanying differential scanning calorimetry (DSC) measurement, which quantifies the heat absorption of a sample relative to a reference, revealed an endothermic feature that we ascribe to a solid-liquid transition, i.e. melting, at 451 °C (ΔH_f = 1.8 kJ mol^{-1}) (**Figure 1b**). Cooling of this liquid to room temperature yielded a vitreous product, termed a_gZIF-76 (**Supplementary Figure 1**). a_gZIF-76 exhibits a glass transition temperature, T_g, of 310 °C upon reheating in a DSC measurement (**Figure 1b, Supplementary Figure 6**).

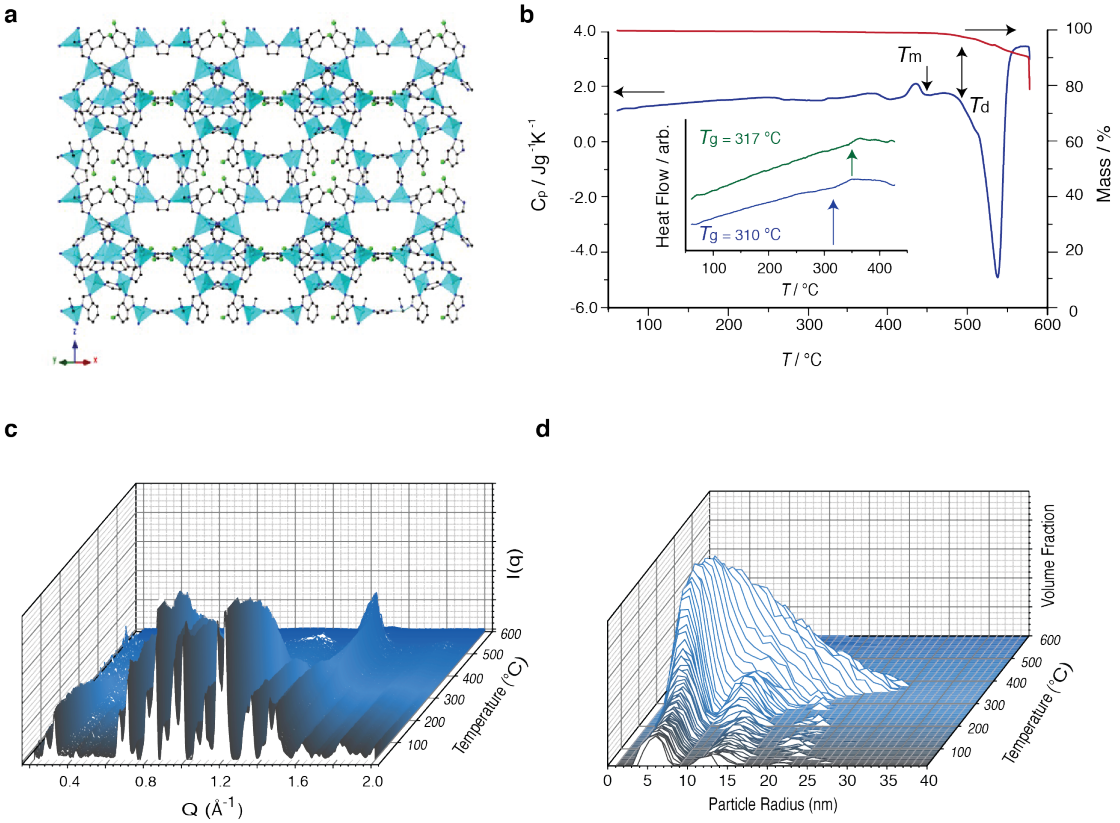

Figure 1. Liquid and Glass Formation of ZIF-76. (a) The structure of ZIF-76, as determined by single-crystal X-ray diffraction.[20] Zn – light blue, Cl – green, C – grey, N – dark blue, H – omitted for clarity. (b) The isobaric heat capacity (C_p) and mass change (%) of ZIF-76 measured during a DSC-TGA upscan at 10 °C/min, highlighting the stable liquid domain between T_m and T_d. Inset – Glass transitions for a_gZIF-76 (blue) and a_gZIF-76-mbIm (green). (c) Temperature resolved WAXS profile of ZIF-76 upon heating from 25 °C to 600 °C. (d) Temperature resolved volume fraction distributions of the different particle sizes of ZIF-76, indicating coalescence into particles of up to 30 nm.

The isostructural framework $[Zn(Im)_{1.33}(5\text{-mbIm})_{0.67}]$ (5-mbIm = 5-methylbenzimidazolate, $C_8H_7N_2$) can be also be formed (**Supplementary Figure 7**).[22,23] This material, referred to as ZIF-76-mbIm, allowed us to study the relationship between ZIF structure and the properties of the resulting glass (a_gZIF-76-mbIm). ZIF-76-mbIm melts at 471 °C (**Supplementary Figure 8**), indicating a higher energy barrier to ligand dissociation due to the electron-donating methyl group. A similar electronic effect was previously pinpointed as the reason why ZIF-8 does not melt.[11] a_gZIF-76-mbIm possesses a T_g of 317 °C (**Figure 1b**, **Supplementary Figure 9)**. The linker ratio of ZIF-76-mbIm, and indeed ZIF-76, are maintained in their respective glasses (**Table 1**, **Supplementary Figures 2-5, 10 and 11**), which is expected on the basis that no mass loss occurs during the melting process. The greater T_g for a_gZIF-76-mbIm is consistent with the greater van der Waals radius of a methyl group compared to chlorine atom, which leads to stronger non-covalent interactions between the framework constituents. This trend is reminiscent of the relationship between T_g and steric side groups in organic polymers.[24,25]

The transformation of ZIF-76 from the crystalline to the liquid state was investigated by small- and wide- angle X-ray scattering (SAXS and WAXS). Bragg diffraction in the variable temperature WAXS pattern decreases sharply around 420 °C, consistent with the melting point from DSC. The resultant diffuse scattering then ceases at *ca*. 520 °C, corresponding to thermal decomposition (**Figure 1c**). The ZIF-76 liquid is therefore stable over a temperature range of approximately 100 °C, consistent with TGA evidence (**Figure 1b**).

Table 1. Summary of the crystalline and glass samples.

	Composition [a]	State	T_m (°C)	T_g (°C)	T_d (°C)
ZIF-76	$[Zn(Im)_{1.62}(5\text{-ClbIm})_{0.38}]$	crystalline	451	-	517
a_gZIF-76	$[Zn(Im)_{1.62}(5\text{-ClbIm})_{0.38}]$	glass	-	310	511
ZIF-76-mbIm	$[Zn(Im)_{1.33}(5\text{-mbIm})_{0.67}]$	crystalline	471	-	596
a_gZIF-76-mbIm	$[Zn(Im)_{1.33}(5\text{-mbIm})_{0.67}]$	glass	-	317	590

The SAXS intensity follows a power law behaviour of the form $Q^{-\alpha}$ at room temperature (**Supplementary Figures 12 and 13**). Fitting gave a value of α = 3.7, which decreased to 3.5 at 360 °C, indicating a roughening of internal surface structure upon melting. Similar results were observed in a previous study of the melting of a different MOF material, ZIF-62.[26] The dynamic nature of the MOF liquid phase upon heating was evidenced by a steady increase in α to 3.9 between 360 °C and 500°C, which we associate with a regularization of the internal pore structure of the liquid with both time and temperature. The discontinuity in the SAXS profile at around 550 °C indicates thermal decomposition, in accordance with the WAXS and DSC measurements. The volume weighted fractions of the particles below the observable limit of 315 nm in the sample were extracted from the data (**Figure 1d**), showing crystalline ZIF-76 particles of 5 nm, 12 nm and 20 nm radius, which coalesce at *ca*. 370 °C before melting at higher temperatures.

Linker Positioning in the Vitreous State

The chemical environments, distribution and relative motion of the framework linkers in the liquid state prior to vitrification were studied, to gain insight into phase separation processes and glass homogeneity. Solid-state ^{1}H magic angle spinning (MAS) NMR spectroscopic measurements were carried out for this purpose. Measurements on an evacuated sample of ZIF-76 yielded a single, broad, unresolvable signal at 6-7 ppm arising from both Im and ClbIm protons (**Supplementary Figure 14**). The spectrum of ZIF-76-mbIm featured an additional peak at 1.5 − 2 ppm, belonging to the methyl substituent of the benzimidazolate ring. The ^{13}C MAS NMR spectra of these crystalline samples exhibited several partly resolved signals**,** matching those expected from the chemical structure of the ligand (**Supplementary Figure 15**). Vitrification resulted in little change to the resonances in both the ^{1}H and ^{13}C spectra, aside from a small shift in position of the methyl group resonance to lower field in the ^{13}C NMR spectrum of ZIF-76-mbIm. These MAS NMR results demonstrate

that the chemical environments of the ligands in the glasses are broadly similar to those in their crystalline precursors.

The distribution of the organic linkers within both crystal and glass phases was also investigated using spin diffusion NMR spectroscopy. This is a powerful technique, which is able to detect the proximity of different organic components based on the rate of polarization transfer between their protons.[27,28] ^{1}H-detected spin-diffusion experiments were first performed on ZIF-76-mbIm, to track the transfer of proton polarization from the methyl group protons of 5-mbIm (resonance at 2 ppm) to all other protons in the sample (with chemical shifts in the region 6-7 ppm). Off-diagonal peaks at a mixing time of 0 ms are absent, as expected. Their appearance and gradual strengthening in intensity after this time however, is due to polarization transfer (**Supplementary Figure 16**). After mixing times of 10-12 ms, a plateau in the spin-diffusion curve (**Supplementary Figure 17**) was observed, indicating that maximum transfer to both imidazolate and other 5-methylbenzimidazolate protons had been achieved. The detection of a well-resolved and isolated ^{1}H signal from the methyl group protons of 5-mbIm and the ^{13}C signal from **C1'** of the Im ligand (**Figure 2a**) facilitated ^{13}C-detected proton spin-diffusion measurements. This allowed us to track the polarization transfer from the methyl group to **H1** protons of the 5-methyl benzimidazolate (intra-linker transfer) and to **H1'** protons of the imidazolate (inter-linker transfer between the two different linkers) (**Figure 2b**). In crystalline ZIF-76-mbIm, the inter-linker transfer of polarization was observed to be faster than intra-linker transfer, implying that the linkers are well mixed within the framework (**Figure 2c)**. In a_gZIF-76-mbIm, very fast spin-diffusion among the linkers of two different types confirms that the 5-methyl benzimidazolate and imidazolate linkers remain very well mixed and do not separate into domains. Notably, the initial parts of the spin-diffusion curves of the glass are steeper than in the crystal, suggesting that the inter-linker distances between 5-methyl benzimidazolate and imidazolate linkers contract slightly upon vitrification (**Figure 2d**). This is consistent with the downfield shift of the methyl group

resonance in the ^{13}C NMR spectrum of a_gZIF-76-mbIm, which may arise from closer contacts with the π electron clouds of neighboring ligands.

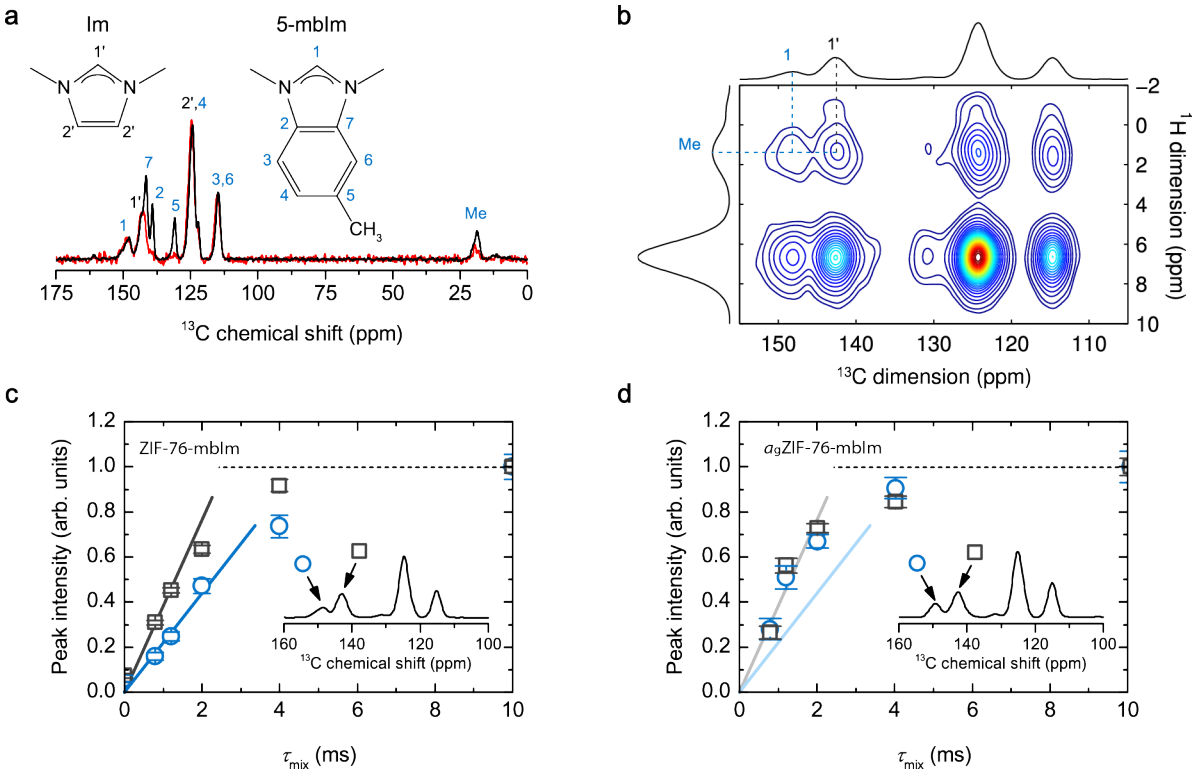

Figure 2. Linker dynamics upon melting. (a) ^{13}C MAS (black solid line) and ^{1}H-^{13}C Lee-Goldburg cross-polarization MAS (red solid line) NMR spectra of crystalline ZIF-76-mbIm. Tentative assignment of individual signals is based on literature data for isotropic chemical shifts from the two molecular fragments. The assignment is further confirmed by comparing the resonances in the ^{13}C MAS and ^{1}H-^{13}C Lee-Goldburg cross polarization MAS NMR spectra. In the latter, only resonances belonging to those carbons with hydrogens attached can be observed. (b) ^{13}C-detected 2D spin-diffusion NMR spectrum, recorded with a mixing time of 10 ms. Cross peaks due to polarization transfer between methyl protons of 5-mbIm on one hand and H1' protons of Im and H1 protons of 5-mbIm on the other are denoted. (c) and (d) Spin-diffusion curves from the ^{13}C-detected measurements on ZIF-76-mbIm and a_gZIF-76-mbIm (squares: inter-linker polarization transfer between methyl protons of 5-mbIm and H1' protons of Im; circles: intra-linker polarization transfer between methyl and H1 protons of 5-mbIm). Solid lines in (c) and (d) indicate the initial slopes of the two spin-diffusion curves for crystalline ZIF-76-mbIm (i.e., lines in (d) are equal to lines in (c)).

Pair Distribution Function Measurements

To further probe the structures of the ZIFs before and after vitrification, synchrotron X-ray total scattering measurements were performed on ZIF-76, ZIF-76-mbIm, a_gZIF-76 and a_gZIF-76-mbIm (**Figure 3a**). The glassy nature of a_gZIF-76 and a_gZIF-76-mbIm was confirmed by the absence of sharp features in their respective structure factors. The corresponding pair distribution function (PDFs), which are in effect atom-atom distance histograms, of all samples were extracted after appropriate data corrections (**Figure 3b**). The PDFs of all samples are near-identical up to 6 Å. Since the correlations in this range are C-C/C-N (1.3 Å) and Zn-N (2 Å and 4 Å), this implies that the local Zn^{2+} environment is near identical in all four samples. The limit of this order, at 6 Å, corresponds to the distance between two Zn^{2+} centres, and confirms that metal-ligand-metal connectivity is present within both crystalline and glass samples. This is consistent with observations made on other MOF glasses, and it underscores the consistency in the composition of these materials and the similar coordination environment of the zinc(II) ions across the crystalline and amorphous phases.[16]

The PDFs of dense ZIF-glasses are relatively featureless beyond 6 Å,[16] which contrasts with the PDFs of a_gZIF-76 and a_gZIF-76-mbIm. In particular, the feature at 7.5 Å in the $D(r)$ for a_gZIF-76 (Peak A, **Figure 3b and inset**) is related to a Zn-N^3 distance, where N^3 is the third nearest N atom to a given Zn^{2+} ion. A further feature at 10.8 Å is related to the distance between a Zn^{2+} ion and the Cl group on the next nearest neighbour ligand (Peak B, **Figure 3b and inset**). The observation of medium range order (MRO) in the glass state, i.e. **Zn**-Im-Zn-**ClbIm** connectivity, is ascribed to the relative sluggish diffusion kinetics and high viscosities of the liquid phase. Lower viscosities associated with greater ligand movement would result in vastly reduced **Zn**-Im-Zn-**ClbIm** correlations.[11] The extended connectivity here would also render a contiguous pore network possible, as confirmed later by gas adsorption. Similar analysis of the PDFs for ZIF-76-mbIm and a_gZIF-76-mbIm (**Supplementary Figure 18**) also indicates a degree of MRO in the glass, with oscillations

persisting to higher *r* values. This is also consistent with the lower position of the first sharp diffraction peak of ZIF-76-mbIm.[29]

Synchrotron X-ray diffraction data were collected during the melting process of ZIF-76 (**Figure 3c**). We observed an irreversible reduction in diffraction intensity upon heating, resulting in complete loss of all sharp diffraction peaks in the *S*(Q) at the highest studied temperature of 540 °C. In the PDF, features at *r* values of over 8-10 Å present in crystalline ZIF-76 gradually, and irreversibly disappear with increasing temperature to become virtually absent by 540 °C (**Figure 3d**).

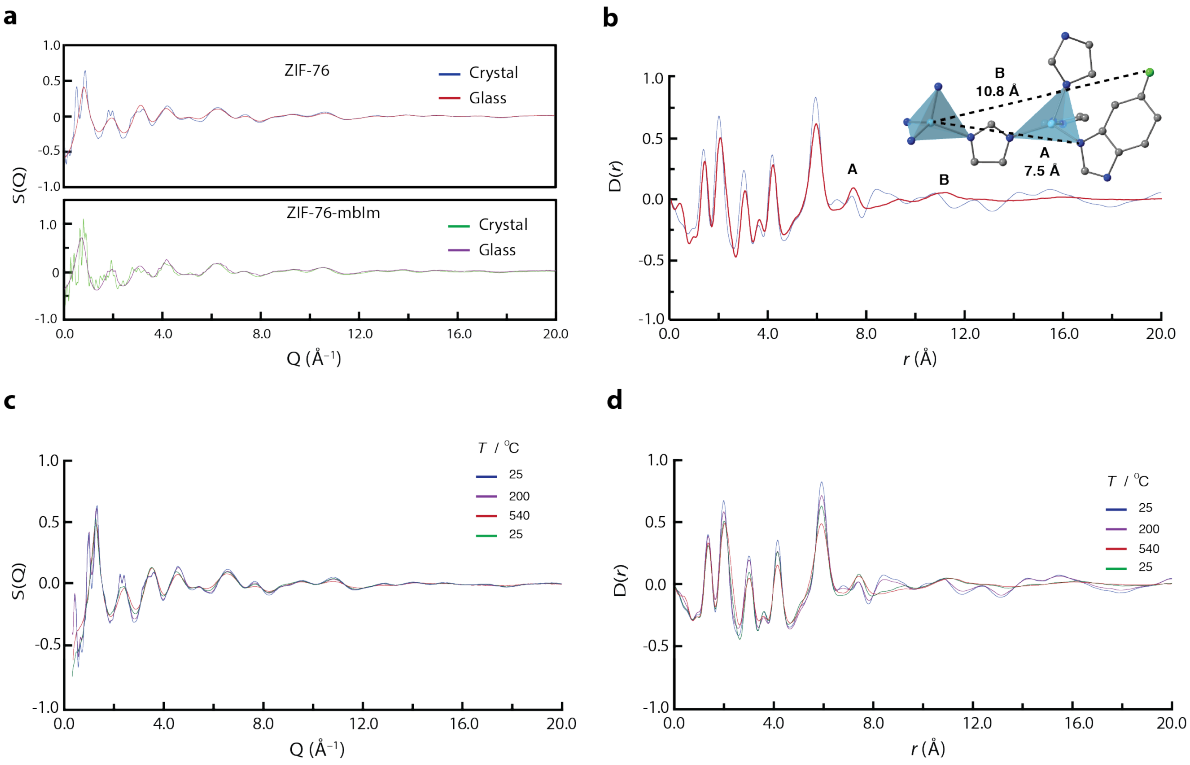

Figure 3. Diffraction in the Crystalline and Glass State. (a) X-ray structure factors *S*(Q) of ZIF-76 and ZIF-76-mbIm, crystalline and glass samples. (b) Corresponding ZIF-76 pair distribution function *D*(r). Inset – medium range order. Zn – light blue, Cl – green, C – grey, N – dark blue, H – omitted for clarity. (c) X-ray structure factors *S*(Q) of ZIF-76 upon heating. (d) Pair distribution functions *D*(r) of ZIF-76 upon heating.

Accessible Porosity in a MOF-glass

We have previously shown that positron annihilation lifetime spectroscopy (PALS) is a useful tool for the mapping of various pore sizes in MOF crystals and glasses.[30] In agreement with the crystal structure of ZIF-76,[20] two cavity diameters of 5.7 Å and 15.7 Å were detected in (**Supplementary Figure 19**, **Supplementary Table 1**). Upon vitrification to a_gZIF-76, a single pore with a diameter of *ca.* 5 Å was revealed. PALS analysis of crystalline ZIF-76-mbIm again yielded two cavities of diameters 5.8 Å and 15.6 Å. The a_gZIF-76-mbIm glass retains two distinct pores with diameters of 4.8 Å and 7.2 Å (**Supplementary Figure 20**). The analysis shows a reduction in porosity due to vitrification, however the glasses, and particularly a_gZIF-76-mbIm, still maintain significant porosity.

To prepare samples possessing high pore volumes before conducting gas adsorption experiments, we optimized the synthetic procedures for ZIF-76 and ZIF-76-mbIm, and incorporated larger quantities of the benzimidazolate-derived linker in each case. This strategy borrows the logic employed by Yaghi et al in the synthesis of new high surface area crystalline materials.[19] Samples of ZIF-76 and ZIF-76-mbIm, with stoichiometries of $[Zn(Im)_{1.0}(5\text{-ClbIm})_{1.0}]$ and $[Zn(Im)_{0.93}(5\text{-mbIm})_{1.07}]$, respectively, were thus prepared. The ligand ratios in these materials were determined by ^{1}H NMR spectroscopy on dissolved samples (**Supplementary Figures 21 and 22**). A range of gas adsorption isotherms were measured on crystalline $[Zn(Im)_{1.0}(5\text{-ClbIm})_{1.0}]$ and $[Zn(Im)_{0.93}(5\text{-mbIm})_{1.07}]$. From N_2 adsorption isotherms at 77 K, BET surface areas of 1313 $cm^2\ g^{-1}$ and 1275 $cm^2\ g^{-1}$ were estimated for ZIF-76 and ZIF-76-mbIm, respectively. These values are consistent with those reported in the literature.[22] As expected, these crystalline ZIFs are also porous to a range of other small gases (**Table 2, Supplementary Figures 23-28 and Supplementary Tables 2-4**).

Remarkably, and representing a departure from the dense melt quenched MOF-glasses reported to date,[16] a_gZIF-76 and a_gZIF-76-mbIm are permanently porous to incoming gases. While a_gZIF-76 reversibly adsorbs in excess of 4 wt% CO_2 at 273 K (**Supplementary Figure 29**), isotherms measured on this glass were accompanied by significant hysteresis in their desorption branches, which persisted with long equilibration times. This indicates restricted diffusion of guest molecules due to constrictions in the pore network, which is consistent with very low uptake of N_2 and H_2 at 77 K. We therefore turned our attention to the permanent porosity displayed by a_gZIF-76-mbIm, which reversibly adsorbs CO_2 and CH_4 at 273 K and 293 K (**Figure 4a**). In this case, the adsorption isotherms exhibited only very minor hysteresis, implying that diffusion limitations are largely absent for these gases. At 77 K, however, N_2 is prevented from diffusing into the pores, while H_2 is adsorbed but with significant hysteresis (**Supplementary Figure 30**).

The appreciable network of accessible, interconnected pores in a_gZIF-76-mbIm enables it to adsorb 7.0 wt% of CO_2 at 273 K and a pressure of 1 bar (**Table 2**). Micropore volumes and surface areas for ZIF-76-mbIm and a_gZIF-76-mbIm were estimated by NLDFT fitting of their CO_2 adsorption isotherms (**Supplementary Figures 31 and 32**). We note that these are naturally lower than the values derived from N_2 isotherms measured at 77 K, which could only be obtained for ZIF-76-mbIm. The lower CO_2 uptake of a_gZIF-76-mbIm compared to its crystalline precursor can be ascribed to the slight contraction of the overall pore volume of 0.12 $cm^3\ g^{-1}$ upon vitrification. The enthalpy of adsorption at Q_{st} for CO_2 indicates that a_gZIF-76-mbIm binds CO_2 more strongly than ZIF-76-mbIm (**Figure 4b, Supplementary Figures 33 and 34**). The modest Q_{st} at zero coverage of the crystalline ZIF (−27.2 kJ mol^{-1}) arises from its largely non-polar pore environment, while the increase in Q_{st} in the glass reveals a pore environment with enhanced interactions with the guest CO_2 molecules (vide infra).

Table 2. Summary of the textural characteristics of a permanent porous glass derived from ZIF-76-mbIm.

		ZIF-76-mbIm	a_gZIF-76-mbIm
Uptake of CO_2 (1 bar, 273 K)		10.0 wt%	6.7 wt%
Surface area [a]	from N_2 / 77 K data	1173	[d]
	from CO_2 / 273 K data	643	375
Pore volume [b]	from N_2 / 77 K data	0.50	[d]
	from CO_2 / 273 K data	0.17	0.12
Isosteric heat of adsorption, Q_{st} (CO_2) [c]		−26.3	−29.3

[a] In $cm^2\ g^{-1}$ using the BET model (N_2) or NLDFT fitting (CO_2). [b] Volume accessible to adsorbate in $cm^3\ g^{-1}$ at 1 bar using the density of liquid adsorbate (N_2) or NLDFT fitting. [c] In kJ mol^{-1} at zero loading. [d] Not measurable due to diffusion limitations.

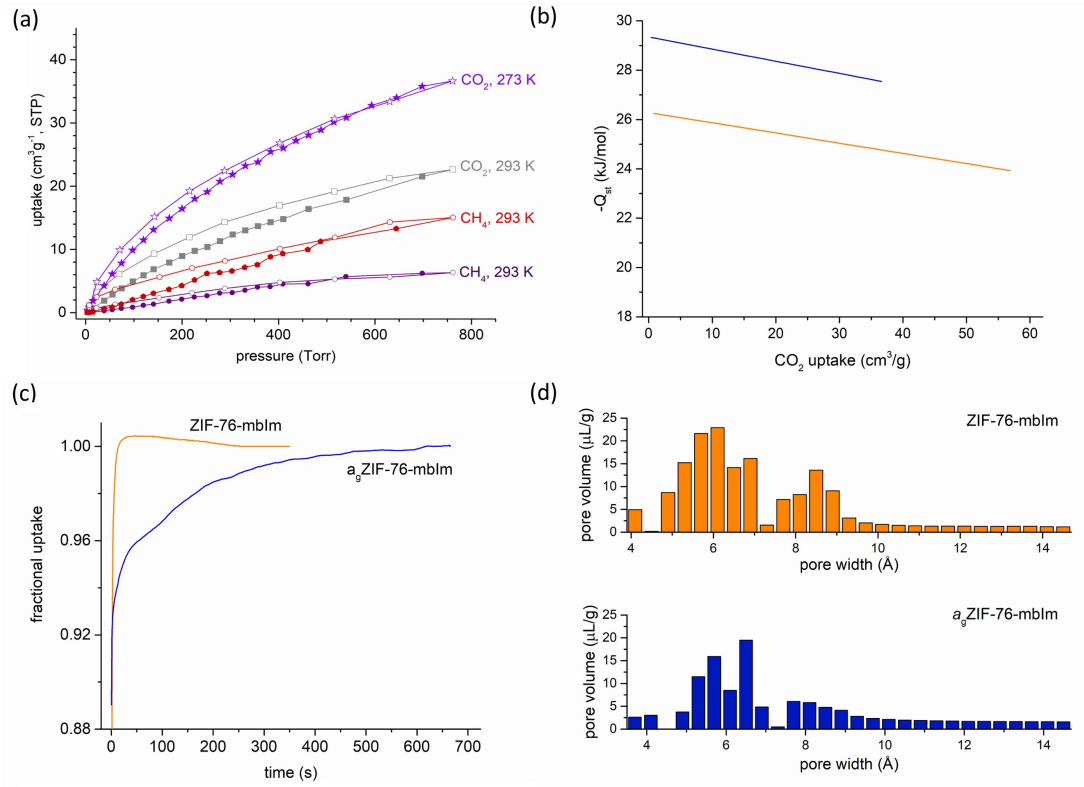

Figure 4. Permanent accessible porosity in a_gZIF-76-mbIm and comparisons with ZIF-76-mbIm. (a) Adsorption isotherms of a_gZIF-76-mbIm (filled symbols = adsorption, empty symbols = desorption), (b) Calculated isosteric heats of adsorption (Q_{st}) for CO_2 as a function of guest loading, orange – ZIF-76, blue – a_gZIF-76-mbIm. (c) Time-dependent CO_2 uptake profiles at 273 K at a pressure of 5 Torr, (d) Pore size distributions as determined by a NLDFT method from CO_2 adsorption isotherms at 273 K.

The kinetic profiles of CO_2 uptake were also measured for ZIF-76-mbIm and a_gZIF-76-mbIm. a_gZIF-76-mbIm takes significantly longer to attain equilibrium between the adsorbed and non-adsorbed gas molecules (**Figure 4c**), which implies that diffusion is more constricted in the glass than its crystalline precursor, and the pore network is more tortuous. This is consistent with the reduced structural regularity inherent in glass, and we ascribe the higher Q_{st} for binding CO_2 of the glass to a highly contoured pore surface. A further illustration of the pore structure is provided by the pore size distribution calculated from CO_2 adsorption isotherms at 273 K, which indicate that the pores contract slightly upon vitrification (**Figure 4d**). Taken together, these observations show that glasses derived from ZIFs have potential in both kinetic and equilibrium-based gas separation processes. Glasses for gas separations may optimised by matching the pore window sized to the kinetic diameters of target gas pairs. Preliminary experiments indicate that this may be accomplished by varying linker ratios in these glasses. Vitrification of the crystalline frameworks is possible within a broad range of linker ratios to produce porous glasses with finely tuned textural characteristics. The adsorption of gases and the separation of gas mixtures using this suite of materials are the subjects of ongoing investigation.

We note that the network of channels in a_gZIF-76-mbIm is stable for at least three months, a conclusion drawn from the reproducibility of adsorption isotherms measured on samples stored over this period of time. Further, the glasses can be handled in ambient laboratory atmospheres without any detrimental effects on their adsorption capacity. The superior textural characteristics of a_gZIF-76-mbIm compared to a_gZIF-76 can be ascribed to the presence of the methyl group in the former. As indicated by solid-state NMR, these groups anchor the glassy lattice by noncovalent interactions with neighbouring ligands, which helps to maintain a relatively open and contiguous network of pores and channels.

Discussion

This report describes permanent, accessible, and reversible porosity inherent to glasses derived from metal-organic frameworks. Two precursor crystalline ZIFs were designed, and their high temperature melting monitored *in-situ* by a range of combined diffraction experiments. Notably, these glasses are distinct from those reported by Yaghi and Angell,[13] which are prepared via sol-gel methods, and in which T_g disappears after solvent evaporation. The discovery of accessible porosity in glasses derived from MOFs may serve as the foundation for a new class of porous hybrid inorganic-organic materials. We expect that developments in this field will be enabled by (i) the large number of known MOF or coordination polymer structures that can serve as potential glass precursors,[31] (ii) the ability to combine the chemical diversity of MOFs with established techniques for handling and moulding glasses, (iii) the availability of several techniques for vitrifying crystalline frameworks,[12,32] and (iv) the use of post-synthetic techniques that are employed in other glass families to increase available surface areas.[33]

We envisage a plethora of potential applications will stem from porous MOF glasses, including membranes for chemical separations, catalysis, ion transport, and conductivity.[34] Additional avenues for research may also arise from their comparison and contextualization with conventional glasses. In this light, MOF glasses may be geared towards applications in optics, where one of their principle advantages will lie in their 'softer' nature and correspondingly lower processing temperatures. The combination of the stimuli responsivity of MOF chemistry[35] with the glass domain will also lead to new, smart applications and a new era of glass technology.[36]

Methods

Synthesis

ZIF-76 [$Zn(Im)_{1.62}(5\text{-ClbIm})_{0.38}$] and ZIF-76-mbIm [$Zn(Im)_{1.33}(5\text{-mbIm})_{0.67}$] were prepared via the procedures reported by Peralta et al in the literature.[22] Specifically, imidazole (0.12 g, 17.25 x 10^{-4} mol) and 5-chlorobenzimidazole (0.13 g, 8.66x10^{-4} mol) were mixed together in a solution of DMF (8.28 mL) and DEF (5.73 mL). $Zn(NO_3)_2.6H_2O$ (0.25 g, 8.59 x 10^{-4} mol) was subsequently added, along with NaOH (0.52 mL, 2.5 moldm^{-3}). The turbid solution was then heated to 90 °C for 5 days, and the microcrystalline powder collected by filtration. Occluded solvent was removed by heating under vacuum at 200 °C for 6 h.[37] For the mbIm equivalent, 5-methylbenzimidazole (0.115 g) was used in place of 5-chloroimidazole. Identical procedures were followed for samples of [$Zn(Im)_{1.0}(5\text{-ClbIm})_{1.0}$] and [$Zn(Im)_{0.93}(5\text{-mbIm})_{1.07}$] except $NaOH_{(aq)}$ was omitted from the reaction solvent.

Vitrification

Bulk powder samples were placed into a ceramic crucible and then into a tube furnace, which was purged with argon, prior to heating at 10 °C/min to the melting temperatures identified in Table 1. Upon reaching the set temperature, the furnace was turned off and the samples allowed to cool naturally (under argon) to room temperature.

X-ray Powder Diffraction

Data were collected with a Bruker-AXS D8 diffractometer using Cu Kα (λ =1.540598 Å) radiation and a LynxEye position sensitive detector in Bragg-Brentano parafocusing geometry.

Total Scattering measurements

X-ray data were collected at the I15-1 beamline at the Diamond Light Source, UK (λ = 0.161669 Å, 76.7 keV). A small amount of the sample was loaded into a borosilicate glass capillary of 1.17 mm (inner) diameter. Data on the sample, empty instrument and capillary were collected in the region of $\sim 0.4 < Q < \sim 26$ Å^{-1}. Background, multiple scattering, container scattering, Compton scattering and absorption corrections were performed using

the GudrunX program.[38,39] Variable temperature measurements were performed using an identical set up, though the capillaries were sealed with araldite. Data were taken upon heating at 25 °C, 100 °C, 200 °C, 280 °C and then in 10 °C steps to 340 °C. Further data were collected in 20 °C intervals to 540 °C, before cooling and a final data set taken at room temperature. Data were corrected using equivalent data those taken from an empty capillary heated to identical temperatures.

Combined small angle – wide angle X-ray scattering

X-ray data were collected at the I22 beamline at the Diamond Light Source, UK (λ = 0.9998 Å, 12.401 keV). The SAXS detector was positioned at a distance of 9.23634 m from the sample as calibrated using a 100 nm period Si_3N_4 grating (Silson, UK), giving a usable Q range of 0.0018 – 0.18 $Å^{-1}$. The WAXS detector was positioned at a distance of 0.16474 m from the sample as calibrated using a standard CeO_2 sample (NIST SRM 674b, Gaithersburg USA), giving a usable Q range of 0.17 – 4.9 $Å^{-1}$. Samples were loaded into 1.5 mm diameter borosilicate capillaries under argon inside a glovebox and sealed to prevent the ingress of air. Samples were heated using a Linkam THMS600 capillary stage (Linkam Scientific, UK) from room temperature to 600°C at 10°C/min. Simultaneous SAXS/WAXS data were collected every 1°C. Data were reduced to 1D using the DAWN package [40,41]and standard reduction pipelines.[42] Values for the power law behavior of the samples were found using the power law model of SASView 4.1.1.[43] Data were fitted over the range 0.003 ≤ Q ≤ 0.005 $Å^{-1}$. Particle size distributions were calculated using the McSAS package,[44,45] a minimal assumption Monte Carlo method for extracting size distributions from small-angle scattering data. Data were fitted over the range 0.002 ≤ Q ≤ 0.18 $Å^{-1}$ with a sphere model.

Nuclear Magnetic Resonance Spectroscopy

Solid-state NMR experiments were carried out on a 600 MHz Varian NMR system equipped with a 1.6 mm Varian HXY MAS probe. Larmor frequencies for ^1H and ^{13}C were 599.50 MHz and 150.74 MHz, respectively, and sample rotation frequency was 40 kHz. For one-dimensional ^1H and ^{13}C magic-angle spinning (MAS) measurements, ^1H and ^{13}C 90° excitation pulses of 1.65 µs and 1.5 µs were used, respectively. In ^1H MAS NMR

measurements 8 scans were co-added and repetition delay between scans was 3 s. In ^{13}C MAS NMR measurements number of scans was 5500 and repetition delay was 30 s. Frequency axes of ^{1}H and ^{13}C spectra were referenced to tetramethylsilane. ^{1}H-^{13}C cross-polarization (CP) MAS NMR experiment employed Lee-Goldburg (LG) CP block with duration of 100 μs and high-power XiX heteronuclear decoupling during acquisition; number of scans was 660 and repetition delay between scans was 0.4 s. For two-dimensional ^{1}H-^{1}H and ^{1}H-^{13}C spin-diffusion measurements the numbers of scans were 16 and 4000, and numbers of increments in indirectly detected dimensions were 100 and 12, respectively. Repetition delay between scans was 0.5 s. During mixing periods of both measurements, RFDR scheme was used to enhance homonuclear dipolar coupling among protons. ^{1}H-^{13}C experiment employed LG scheme during the CP block.

Solution ^{1}H NMR spectra of digested samples (in a mixture of DCl (35%)/D_2O (0.1 mL) and DMSO-d_6 (0.5 mL)) of samples (about 6 mg) were recorded on a Bruker Avance III 500MHz spectrometer at 293 K. Chemical shifts were referenced to the residual protio-solvent signals of DMSO-d_6. The spectra were processed with the MestreNova Suite.

Differential Scanning Calorimetry and Thermogravimetric Analysis

Characterizations of all the samples were conducted using a Netzsch STA 449 F1 instrument. The samples were placed in a platinum crucible situated on a sample holder of the DSC at room temperature. The samples were heated at 10 °C /min to the target temperature. After natural cooling to room temperature, the second upscan was performed using the same procedure as for the first. To determine the C_p of the samples, both the baseline (blank) and the reference sample (sapphire) were measured.[46]

Gas Adsorption

Isotherms were measured by a volumetric method using a Quantachrome Autosorb iQ2 instrument with ultra-high purity gases. Prior to analysis, the samples were degassed under a dynamic vacuum at 10^{-6} Torr for 10 hours at 150 °C. Accurate sample masses were calculated using degassed samples after sample tubes were backfilled with nitrogen. Where

possible, BET surface areas were calculated from N_2 adsorption isotherms at 77 K according to established procedures.[47]

Density Measurements

True densities were measured using a Micromeritics Accupyc 1340 gas pycnometer (1 cm^3 model). The typical mass used was 0.2 g, with the values quoted being the mean and standard deviation from a cycle of 10 measurements.

Positron Annihilation Lifetime Spectroscopy

^{22}NaCl, sealed in a thin Mylar envelope, was used as the source of positrons. The samples were packed to 2 mm thickness surrounding the positron source. The ***o***-Ps lifetime measurements were taken under vacuum (1×10^{-5} Torr) at 298 K using an EG&G Ortec spectrometer at a rate of 4.5×10^6 counts per sample. The lifetimes were converted to pore sizes by using the quantum-based formulation assuming a spherical pore geometry.[48] A full description of the technique can be found in a previous study.[30]

Molecular Simulations

Grand canonical Monte Carlo (GCMC) simulations were performed as implemented in the RASPA simulation code[49] to compute single component gas adsorption isotherms of Ar (77 K), CH_4 (273 K), CO_2 (273 K), H_2 (77K), N_2 (77 K) and O_2 (273 K) in ZIF-76 up to 1 bar. The crystal structure of ZIF-76 [$Zn(Im)_{1.5}(clbIm)_{0.5}$] was taken from the Cambridge Crystallographic Data Center (reference code = GITWEM), and the disorder was removed manually to generate a suitable set of input coordinates for the calculations.[50] Structural properties such as accessible pore volume, pore limiting diameter (PLD) and the largest cavity diameter (LCD) were calculated using Zeo++ software[51] and are listed in **Supplementary Table 4**. For pore volume calculations, the probe radius was set to zero.

Data Availability

The data that support the findings of this study are available from the corresponding authors on request.

Author Acknowledgements

TDB would like to thank the Royal Society for a University Research Fellowship, and for their support (UF150021). We acknowledge the provision of synchrotron access to Beamline I22 (exp. NT18236-1) at the Diamond Light Source, Rutherford Appleton Laboratory UK. We also thank Diamond Light Source for access to beamline I15-1 (EE171151). CZ acknowledges the financial support from the China Scholarship Council and the Elite Research Travel Scholarship from the Danish Ministry of Higher Education and Science. AK and GM acknowledge the support of the Slovenian Research Agency (research core funding No. P1-0021). CMD is supported by the Australian Research Council (DE140101359). LL would like to thank the EPSRC for an allocated studentship. CWA would like to thank the Royal Society for a PhD studentship (RG160498), and the Commonwealth Scientific and Industrial Research Organization (CSIRO) for additional support (C2017/3108). OTQ acknowledges the RSNZ Marsden Fund grant MAU1411. The authors gratefully acknowledge assistance from Dr. Shichun Li in data collection.

Author Contributions

TDB designed the project and wrote the manuscript with SGT, and input from all authors. SAXS/WAXS experiments were performed by TDB, AJS, NJT and GJS, with analysis by AJS and GJS. DSC measurements and sample preparation were carried out by CZ, facilitated by YY. PDF measurements carried out by TDB, DAK, CA, LL, CWA and PAC. All gas adsorption measurements were carried out by SGT, OTQ and SJL. Liquid NMR data were provided by AQ, and solid state NMR measurements carried out and analysed by GM and AK. All simulations were carried out and analysed by IE. PALS data were collected and analysed by CMD, AWT and AJH.

Competing Interests

There are no competing interests.

References

1 Enke, D., Janowski, F. & Schwieger, W. Porous glasses in the 21st century - a short review. *Micropor Mesopor Mat* **60**, 19-30 (2003).

2 Janowski, F. & Enke, D. *Porous Glasses, in Handbook of Porous Solids (eds F. Schüth, K. S. W. Sing and J. Weitkamp)*. (2002).

3 Shimizu, T. *et al.* Transparent, Highly Insulating Polyethyl- and Polyvinylsilsesquioxane Aerogels: Mechanical Improvements by Vulcanization for Ambient Pressure Drying. *Chem Mater* **28**, 6860-6868 (2016).

4 Han, S. H. *et al.* Thermally Rearranged (TR) Polybenzoxazole: Effects of Diverse Imidization Routes on Physical Properties and Gas Transport Behaviors. *Macromolecules* **43**, 7657-7667 (2010).

5 McKeown, N. B. & Budd, P. M. Polymers of intrinsic microporosity (PIMs): organic materials for membrane separations, heterogeneous catalysis and hydrogen storage. *Chem Soc Rev* **35**, 675-683 (2006).

6 Schneermann, A. *et al.* Flexible metal–organic frameworks. *Chem Soc Rev* **43**, 6062-6096 (2014).

7 Horike, S., Shimomura, S. & Kitagawa, S. Soft porous crystals. *Nature Chemistry* **1**, 695-704 (2009).

8 Dissegna, S., Epp, K., Heinz, W. R., Kieslich, G. & Fischer, R. A. Defective Metal-Organic Frameworks. *Adv Mater*, 1704501 (2018).

9 Cliffe, M. J. *et al.* Correlated defect nanoregions in a metal-organic framework. *Nat Commun* **5**, 4176 (2014).

10 Bennett, T. D., Cheetham, A. K., Fuchs, A. H. & Coudert, F. X. Interplay between defects, disorder and flexibility in metal-organic frameworks. *Nature Chemistry* **9**, 11-16 (2017).

11 Gaillac, R. *et al.* Liquid Metal-Organic Frameworks. *Nat Mater* **16**, 1149-1154 (2017).

12 Chen, W. Q. *et al.* Glass Formation of a Coordination Polymer Crystal for Enhanced Proton Conductivity and Material Flexibility. *Angew Chem Int Edit* **55**, 5195-5200 (2016).

13 Zhao, Y., Lee, S.-Y., Becknell, N., Yaghi, O. M. & Angell, C. A. Nanoporous Transparent MOF Glasses with Accessible Internal Surface. *J Am Chem Soc* **138**, 10818–10821 (2016).

14 Phan, A. *et al.* Synthesis, Structure, and Carbon Dioxide Capture Properties of Zeolitic Imidazolate Frameworks. *Accounts Chem Res* **43**, 58-67 (2010).

15 Tian, Y. Q. *et al.* Design and generation of extended zeolitic metal-organic frameworks (ZMOFs): Synthesis and crystal structures of zinc(II) imidazolate polymers with zeolitic topologies. *Chem-Eur J* **13**, 4146-4154 (2007).

16 Bennett, T. D. *et al.* Melt-Quenched Glasses of Metal-Organic Frameworks. *J Am Chem Soc* **138**, 3484-3492 (2016).

17 Umeyama, D., Horike, S., Inukai, M., Itakura, T. & Kitagawa, S. Reversible Solid-to-Liquid Phase Transition of Coordination Polymer Crystals. *J Am Chem Soc* **137**, 864-870 (2015).

18 Nagarkar, S. S. *et al.* Enhanced and Optically Switchable Proton Conductivity in a Melting Coordination Polymer Crystal. *Angew Chem Int Edit* **56**, 4976-4981 (2017).

19 Yang, J. *et al.* Principles of Designing Extra-Large Pore Openings and Cages in Zeolitic Imidazolate Frameworks. *J Am Chem Soc* **139**, 6448-6455 (2017).

20 Banerjee, R. *et al.* High-throughput synthesis of zeolitic imidazolate frameworks and application to CO2 capture. *Science* **319**, 939-943 (2008).
21 Bennett, T. D. *et al.* Hybrid glasses from strong and fragile metal-organic framework liquids. *Nat Commun* **6**, 8079 (2015).
22 Peralta, D., Chaplais, G., Simon-Masseron, A., Barthelet, K. & Pirngruber, G. D. Synthesis and adsorption properties of ZIF-76 isomorphs. *Micropor Mesopor Mat* **153**, 1-7 (2012).
23 Wu, T., Bu, X. H., Zhang, J. & Feng, P. Y. New Zeolitic Imidazolate Frameworks: From Unprecedented Assembly of Cubic Clusters to Ordered Cooperative Organization of Complementary Ligands. *Chem Mater* **20**, 7377-7382 (2008).
24 Bondi, A. van der Waals Volumes and Radii *The Journal of Physical Chemistry* **68**, 441-451 (1964).
25 Kunal, K., Robertson, C. G., Pawlus, S., Hahn, S. F. & Sokolov, A. P. Role of Chemical Structure in Fragility of Polymers: A Qualitative Picture. *Macromolecules* **41**, 7232-7238 (2008).
26 Longley, L. *et al.* Liquid Phase Blending of Metal-Organic Frameworks. *Nat Commun* **9**, 2135 (2018).
27 Krajnc, A., Kos, T., Logar, N. Z. & Mali, G. A Simple NMR Based Method for Studying the Spatial Distribution of Linkers within Mixed-Linker Metal–Organic Frameworks. *Angew Chem Int Ed Engl* **54**, 10535-10538 (2015).
28 Krajnc, A., Bueken, B., De Vos, D. & Mali, G. Improved resolution and simplification of the spin-diffusion-based NMR method for the structural analysis of mixed-linker MOFs. *Journal of Magnetic Resonance* **279**, 22-28 (2017).
29 Salmon, P. S. & Zeidler, A. Identifying and characterising the different structural length scales in liquids and glasses: an experimental approach. *Phys Chem Chem Phys* **15**, 15286-15308 (2013).
30 Thornton, A. W. *et al.* Porosity in metal–organic framework glasses. *Chem Commun* **52**, 3750-3753 (2016).
31 Moghadam, P. Z. *et al.* Development of a Cambridge Structural Database Subset: A Collection of Metal-Organic Frameworks for Past, Present, and Future. *Chem Mater* **29**, 2618-2625 (2017).
32 Bennett, T. D. & Cheetham, A. K. Amorphous Metal-Organic Frameworks. *Accounts Chem Res* **47**, 1555-1562 (2014).
33 Elmer, T. H. *Engineered Materials Handbook* Vol. 4, Ceramics and Glasses 427-432 (1992).
34 Furukawa, H., Cordova, K. E., O'Keeffe, M. & Yaghi, O. M. The Chemistry and Applications of Metal-Organic Frameworks. *Science* **341**, 974-986 (2013).
35 Coudert, F. X. Responsive Metal–Organic Frameworks and Framework Materials: Under Pressure, Taking the Heat, in the Spotlight, with Friends. *Chem Mater* **27**, 1905-1916 (2015).
36 Morse, D. L. & Evenson, J. W. Welcome to the Glass Age. *Int J Appl Glass Sci* **7**, 409-412 (2016).
37 Prez-Pellitero, J. *et al.* Adsorption of CO2, CH4, and N2 on Zeolitic Imidazolate Frameworks: Experiments and Simulations. *Chemistry: A European Journal* **16**, 1560-1571 (2010).

38 Soper, A. K. GudrunN and GudrunX: Programs for Correcting Raw Neutron and X-ray Diffraction Data to Differential Scattering Cross Section. *Tech. Rep. RAL-TR-2011-013* (2011).
39 Soper, A. K. & Barney, E. R. Extracting the pair distribution function from white-beam X-ray total scattering data. *Journal of Applied Crystallography* **44**, 714-726 (2011).
40 Basham, M. *et al.* Data Analysis WorkbeNch (DAWN). *J Synchrotron Radiat* **22**, 853-858 (2015).
41 Filik, J. *et al.* Processing two-dimensional X-ray diffraction and small-angle scattering data in DAWN 2. *J Appl Crystallogr* **50**, 959-966 (2017).
42 Pauw, B. R., Smith, A. J., Snow, T., Terrill, N. J. & Thünemann, A. F. The modular small-angle X-ray scattering data correction sequence. *Journal of Applied Crystallography* **50**, 1800-1811 (2017).
43 SasView version 4.1 (2017).
44 Pauw, B. R., Pedersen, J. S., Tardif, S., Takata, M. & Iversen, B. B. Improvements and considerations for size distribution retrieval from small-angle scattering data by Monte Carlo methods. *J Appl Crystallogr* **46**, 365-371 (2013).
45 Bressler, I., Pauw, B. R. & Thünemann, A. F. McSAS: software for the retrieval of model parameter distributions from scattering patterns. *Journal of Applied Crystallography* **48**, 962-969 (2015).
46 Yue, Y. Z. The iso-structural viscosity, configurational entropy and fragility of oxide liquids. *J Non-Cryst Solids* **355**, 737-744 (2009).
47 Walton, K. S. & Snurr, R. Q. Applicability of the BET method for determining surface areas of microporous metal-organic frameworks. *J Am Chem Soc* **129**, 8552-8556 (2007).
48 Tao, S. J. Positronium Annihilation in Molecular Substances. *The Journal of Chemical Physics* **56**, 5499 (1972).
49 Dubbeldam, D., Calero, S., Ellis, D. E. & Snurr, R. Q. Raspa: Molecular Simulation Software for Adsorption and Diffusion in Flexible Nanoporous Materials. *Mol. Simul.* **42**, 81–101 (2016).
50 Allen, F. H. The Cambridge Structural Database: a quarter of a million crystal structures and rising. *Acta Crystallogr., Sect. B: Struct. Sci.* **58**, 380-388 (2002).
51 Willems, T. F., Rycroft, C. H., Kazi, M., Meza, J. C. & Haranczyk, M. Algorithms and Tools for High-Throughput Geometry-Based Analysis of Crystalline Porous Materials. *Microporous and Mesoporous Mater.* **149**, 134–141 (2012).